

Continuous wave multi-pass imaging flow cytometry

Yonatan Israel,¹ Joshua L. Reynolds,² Brannon B. Klopfer,² and Mark A. Kasevich^{1,2}

¹*Physics Department, Stanford University, Stanford, California 94305, USA*

²*Applied Physics Department, Stanford University, Stanford, California 94305, USA*

We present a wide-field multi-pass implementation of label-free imaging flow cytometry. Our technique is shown for high-speed flow imaging of ensembles of human red blood cells with up to four passes, demonstrating x4 enhancement in contrast and signal-to-noise. We show that our technique approaches close to the quantum limit of measurement sensitivity, extending the range of optimal imaging to samples in the weakly absorbing regime. This allows for near optimal imaging sensitivity and throughput in a practical scenario of imaging a dynamic sample under limited illumination intensity, surpassing the sensitivity achieved with currently available quantum light sources.

I. INTRODUCTION

Label-free imaging techniques measuring weak optical properties, e.g., the phase shift and absorption due to a thin biological specimen, are typically limited in sensitivity. In the common case where instrumental and environmental noises are negligible, such optical imaging techniques are fundamentally limited by photon shot-noise [1, 2]. By utilizing quantum properties of light, quantum imaging protocols have been proposed and realized for various label-free imaging techniques in order to enhance their sensitivity [3, 4], for example in phase microscopy [5], absorption microscopy [6], and nonlinear microscopy [7, 8]. While these techniques promise enhanced sensitivity, their implementation has so far remained limited and impractical compared to classical imaging techniques.

Multi-pass microscopy is an alternative route to enhancing sensitivity that has recently been investigated [9, 10]. In multi-pass imaging, the optical probe field transits the image target multiple times, increasing the phase shift and absorption of the probe field, which results in an increase in the signal-to-noise ratio (SNR). In this work, we demonstrate that a multi-pass approach can enhance the image sensitivity in a practical scenario of shot-noise limited imaging of a dynamic flow sample.

Such dynamic samples are common in biological imaging, where the objects being imaged either evolve over time or move quickly through the field-of-view of the imaging system. In particular, imaging flow cytometry uses fast flow rates for high throughput characterization and sorting of large cell populations in biological research and clinical diagnostics [11–13]. In such scenarios, the imaging speed must be faster than the sample dynamics to avoid blur, which, for a limited illumination source intensity, results in limited imaging sensitivity due to shot-noise.

In this work, we describe a wide-field multi-pass imaging approach that enhances the sensitivity of label-free imaging flow cytometry. While previous multi-pass microscopes relied on pulsed illumination and time-gated cameras to form the multi-pass image [9, 10], our implementation is compatible with continuous-wave (CW) illumination and conventional cameras. Furthermore, it can accommodate spatially and temporally incoherent

sources, suppressing spurious contributions from out-of-focal-plane scattering, and can achieve up to four passes through the sample. While scanned-cavity methods, such as those described in Refs. [14, 15], can achieve significantly greater signal enhancements, they cannot operate with incoherent illumination or in wide-field, which allows substantially faster image acquisition times.

II. METHODS

The basic CW multi-pass configuration is illustrated in Fig. 1. In this implementation, the imaging beam from an incoherent LED transits a self-imaging optics path either two or four times, depending on the optics configuration.

For a two-pass implementation, illumination light is incoupled through a non-polarizing beamsplitter (BS). The illumination field is focused in the sample region with objective O2. After transiting the sample, the light is collected by objective O1. These fields are then imaged by a tube lens TL1 onto a reflective planar mirror M1. By symmetry, this reflected image is reimaged onto the sample when appropriately aligned. Ray-traces of the relevant optical paths are also shown in Fig. 1. In order to tune the focus, both the O1 objective and sample stage are actuated along the optical axis with encoded piezo stages.

A four-pass implementation utilizes a polarizing beam splitting cube (PBS) and a quarter-wave plate ($\lambda/4$, QWP). In this case, the linear polarization of the beam is rotated by $\pi/2$ as it passes twice through QWP, resulting in redirection of the retroreflected field (after having passed twice through the sample) onto a planar mirror M2. This mirror reflects the fields back into the microscope optical path as in the two-pass implementation. After two more passes through the QWP (four total passes through the sample), the beam exits the microscope and enters the image-forming optics. We toggle between the two-pass and four-pass configurations by adjusting QWP: rotating the polarization of the retroreflection leads to 4 passes, while not rotating it leads to 2 passes. We note that for high NA CW illumination of an isotropic sample, the maximum number of passes is limited to four since

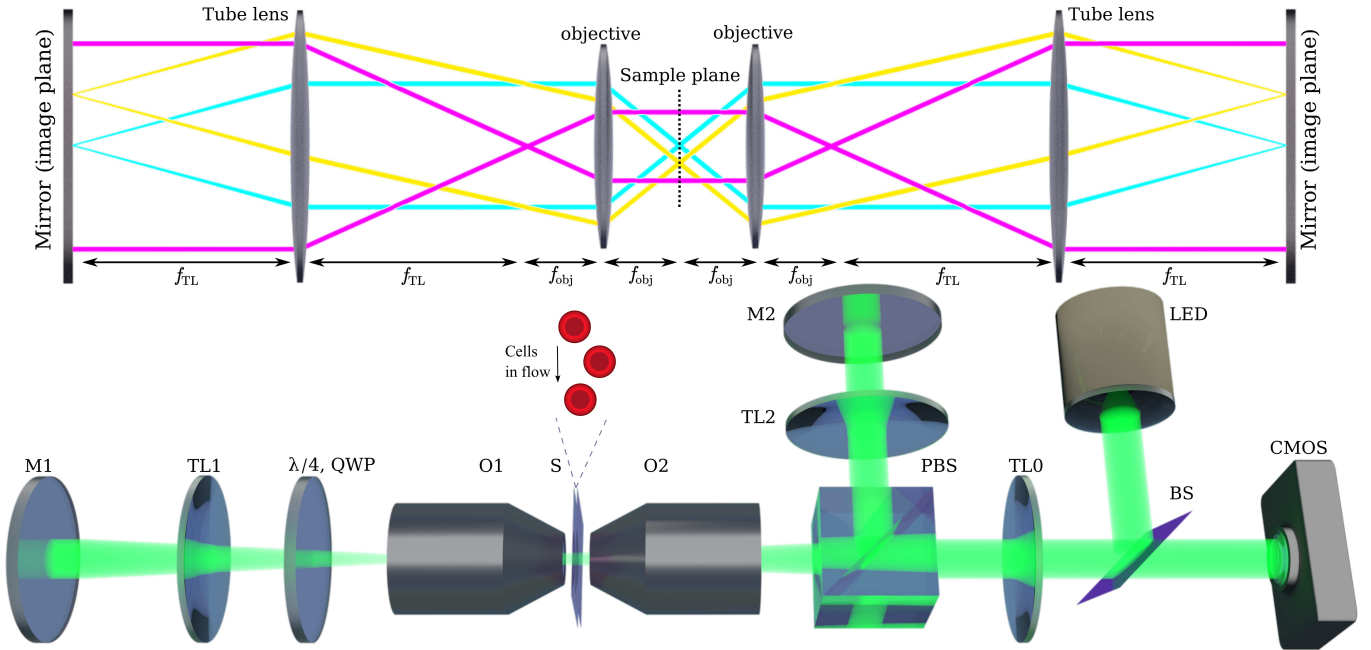


FIG. 1. Multi-pass imaging schematics. **Top:** ray trace of a multi-pass microscope with tube lens and objective focal lengths f_{TL} , f_{obj} , respectively. Rays are shown for plane wave illumination (magenta), on-axis point scatterer (cyan), and off-axis point scatterer (yellow). **Bottom:** optical setup, consisting of two microscopes placed between end mirrors M1 (2). The microscopes consist of NA=0.8 objectives (O1 and O2) and a tube lens (TL1 and TL2). The light (LED) is in- and outcoupled via a beamsplitter (BS) and a polarizing beamsplitter (PBS). A quarter-waveplate ($\lambda/4$, QWP) is used to switch between $m = 2$ and 4 interrogations. $m = 1$ is obtained by severely defocusing the left-hand objective O1. For clarity, additional extracavity optics are omitted.

the polarization has rotated by $\pi/2$ for every round trip through the re-imaging cavity.

To operate the apparatus in an $m = 1$ configuration (i.e. without multi-passing the sample), we operate in the $m = 2$ configuration and severely defocus the objective O1 (see Fig. 1). In this configuration the sample is re-illuminated with a defocused image of the sample, and only objective O2 forms an image on the camera. Thus, we form all images at $m = 1, 2$ and 4 using an identical light source (Thorlabs M530F2), CMOS camera (Teledyne FLIR BFS-U3-32S4M-C), objectives (Zeiss, Plan-Apochromat 20x/0.8), and other optics.

III. SENSITIVITY ANALYSIS

A. Signal-to-noise

To describe the SNR in bright-field multi-pass imaging, assuming in the following an absorption-only sample (ignoring other optical losses), we use the average number of detected photons:

$$\langle \hat{n}(x, y) \rangle = \langle \hat{n}(x, y) \rangle_{in} \cdot \eta^m(x, y), \quad (1)$$

where $\langle \hat{n}(x, y) \rangle_{in}$ is the average number of photons at the apparatus input, $\eta(x, y)$ and $1 - \eta(x, y)$ are the optical transmission and absorption of the specimen, respectively, at transverse positions x and y , and m is the

number of passes. For a measurement at the shot-noise limit, the image SNR is then given by

$$\text{SNR}_m = \frac{|\langle \hat{n} \rangle_{in} - \langle \hat{n} \rangle|}{\sqrt{\langle \hat{n} \rangle_{in} + \langle \hat{n} \rangle}} = \frac{\sqrt{\langle \hat{n}(x, y) \rangle_{in}} \cdot (1 - \eta^m)}{\sqrt{1 + \eta^m}}. \quad (2)$$

For weakly absorbing (high transmissivity) samples, the image SNR is

$$\text{SNR}_m \approx \sqrt{\frac{\langle \hat{n} \rangle_{in}}{2}} \cdot \alpha z \cdot m, \quad (3)$$

where α is the sample absorption per unit depth, related to the transmission by $\eta = e^{-\alpha z}$, and z is the sample thickness. The SNRs of absorption measurements in multi-pass imaging are thus enhanced by a factor m . We note that for imaging at fixed SNR, the required number of detected photons decreases by a factor of m^2 . While we describe here the simple case of an absorption-only sample, multi-pass imaging can also be used to enhance phase contrast as well (see Supplement 1).

B. Fisher Information

Next, we calculate the amount of information about the sample that is carried out by the probe light. We evaluate the effectiveness of imaging flow cytometry for

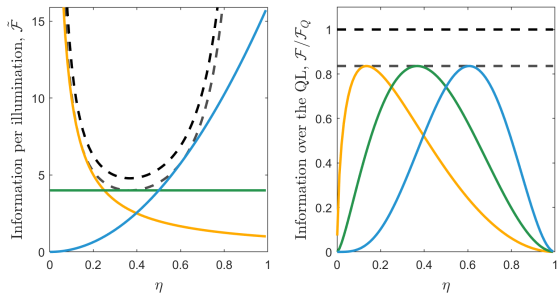


FIG. 2. Limits to absorption information. **Left:** information per illumination, and **Right:** information relative to the quantum limit (QL), for single-pass (gold), two passes (green), and four passes (blue). The quantum $\tilde{\mathcal{F}}_Q$ (dashed black) and the classical limit $\tilde{\mathcal{F}}_{m_{\text{opt}}}$ (dashed gray) on information are shown for comparison.

multi-pass setups and compare it with the quantum limit for information per illumination intensity. The information contained on η in the quantum state of light ρ_η is denoted as \mathcal{F} and known as the quantum Fisher information (QFI) [16–18]. The QFI bounds the measured variance of the absorption according to the quantum Cramér-Rao bound (QCRB),

$$\mathcal{F}(\rho_\eta) \underset{\text{QCRB}}{\geq} 1/\text{Var}(\eta). \quad (4)$$

To compare different experimental strategies we use the QFI per (input) illumination average photon number $\tilde{\mathcal{F}} = \mathcal{F}/\langle \hat{n} \rangle_{\text{in}}$. Using classical light, for multi-pass we have [1, 19]

$$\tilde{\mathcal{F}}_m = m^2 \eta^{m-2}. \quad (5)$$

In particular, the single-pass QFI limited by the (classical) illumination average photon number is given by $\tilde{\mathcal{F}}_1 = 1/\eta$. We note that in Eq. 5, the QFI bounding $\text{Var}(\eta)$ scales with the number of passes similarly to $1/\text{SNR}^2 \sim 1/\langle \hat{n} \rangle_{\text{in}}$ of Eq. 3. Furthermore, we show in Supplement 1 that the variance in η using intensity measurements in our multi-pass setup (Eq. 1) saturates the QFI for multi-pass using classical light $\tilde{\mathcal{F}}_m$ (Eq. 5). By permitting m to be continuous, we find the maximal multi-pass QFI $\tilde{\mathcal{F}}_{m_{\text{opt}}} = 4/(e \cdot \eta \ln \eta)^2$ for $m_{\text{opt}} = -2/\ln \eta$. Note that non-sample losses are ignored, which would reduce the QFI by a factor depending on these losses [1, 19].

To compare the capability of the above techniques, which use classical light, with the absolute upper limit allowed by using quantum light as well as multi-pass approaches, we derive the quantum limit (see Supplement 1),

$$\tilde{\mathcal{F}}_Q \approx \frac{0.65}{(\eta \ln \eta)^2}. \quad (6)$$

It is interesting to note that under constant illumination, an optimal quantum probe allows for a maximal

reduction in variance over an optimal classical multi-pass strategy by $\text{Var}(\eta)_Q/\text{Var}(\eta)_{Cl} = \tilde{\mathcal{F}}_{m_{\text{opt}}}/\tilde{\mathcal{F}}_Q = 0.84$. Quantum light sources are typically orders of magnitude less intense than classical light sources, and quantum approaches are, therefore, currently less sensitive than classical ones. For low-intensity illumination of damage-sensitive samples, quantum light has enabled at most a $\times 1.4$ performance enhancement over single-pass classical strategies [7, 21]. Furthermore, it was recently shown that classical light in a ring resonator can achieve the quantum limit for absorption measurement [22]. While such an approach is not directly applicable for wide-field imaging using incoherent light, an optimized cascaded interferometer could potentially extend the sensitivity of multi-pass and achieve the quantum limit in imaging using classical light [23, 24].

Fig. 2 shows the QFI under fixed illumination intensity and the QFI over the quantum limit for single-pass and multi-pass. While single-pass measurements approach the classical limit, or 84% of the quantum limit for strongly absorbing signals with $\eta \approx 0.13$, four-pass measurements approach these limits for weakly absorbing samples with $\eta \approx 0.61$ ($\eta^m \approx 0.13$). Furthermore, four-pass still maintain a 16-fold increase in information over single-pass for the weak absorption limit $\eta \rightarrow 1$.

IV. RESULTS & DISCUSSION

We first demonstrate multi-pass enhancement with a static sample. Micrographs of a human red blood cell (HRBC), normalized to the average background photon count at $m = 1, 2$, and 4 are shown in Fig. 3, along with lateral cross sections, which are averaged over 20 camera

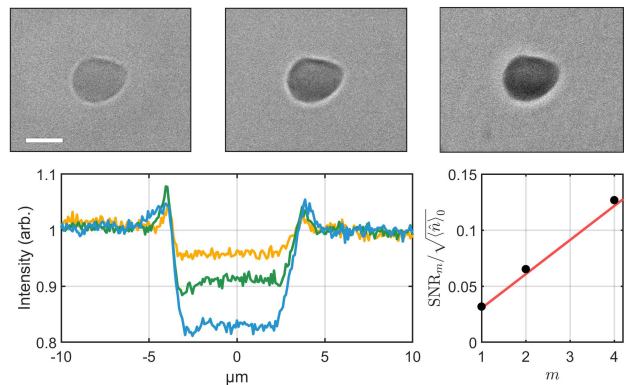


FIG. 3. SNR enhancement for a single static human red blood cell (HRBC). **Top:** bright-field micrographs of a single HRBC at (left to right) $m = 1, 2$, and 4. The images are normalized to the average background squared-root photon flux for each m . Scale bar is $5 \mu\text{m}$. **Bottom left:** lateral cross sections at $m = 1$ (gold), 2 (green), and 4 (blue) showing contrast enhancement. **Bottom right:** SNR after m passes, normalized to the average squared-root photon flux without the object, compared with Eq. 3 for $\eta = 0.957$.

pixels ($\approx 1.7\ \mu\text{m}$ in the sample plane) along the vertical image direction. The gray intensity scale is constant across the three images, and the contrast enhancement is readily visible. The cross sections display approximately linear buildup in contrast as a function of the number of interrogations, as expected for absorption contrast. The measured SNRs use the average squared-root photon flux without the object $\langle \hat{n} \rangle_0$, which accounts for optical losses other than in the sample, instead of the average input photon number $\langle \hat{n} \rangle_{\text{in}}$ used in Eq. 3. The SNR normalized by $\sqrt{\langle \hat{n} \rangle_0}$, $\text{SNR}_m / \sqrt{\langle \hat{n} \rangle_0}$, is averaged over each HRBC image; as shown in Fig. 3, it increases linearly with m , consistent with Eq. 3. We estimate the average HRBC transmission shown in Fig. 3 to be $\eta = 0.957$, while the average SNR_m is measured to be 0.99, 2.1, and 3.6 at $m = 1, 2$, and 4, respectively. The sub-linear enhancement in SNR results from optical losses (see Supplement 1).

When the image acquisition time and illumination intensity are limited, as is the case of imaging flow cytometry, the image SNR is limited. For a 1 mW source illuminating a sample in wide-field and detected using a few mega-pixel camera within an $10\ \mu\text{s}$ exposure time, each pixel records $\langle \hat{n} \rangle_0 \approx 1000$ photons. For such values of $\langle \hat{n} \rangle_0$, the SNR in single-pass imaging is $\text{SNR}_1 \approx 1$ (see Eq. 2) for a weakly absorbing sample having $\eta \approx 0.95$. This SNR can be increased by a factor of 4 by multi-passing a probe with fixed illumination. Alternatively, the required acquisition time necessary to image at fixed SNR would decrease by a factor of 16 for $m = 4$ over a single-pass measurement for a fixed illumination intensity.

To demonstrate the applicability of multi-pass to high-throughput applications such as imaging flow cytometry, we imaged HRBCs flowing through a glass rectangular capillary with a channel depth of $20\ \mu\text{m}$. Sample cells in flow are shown in Fig. 4, where the photon count in each pixel $\langle \hat{n} \rangle$ is normalized to its average value measured in the absence of flowing cells $\langle \hat{n} \rangle_0$, and the gray intensity scale is the same across all images. For our depth-of-field, both in-focus and out-of-focus cells are visible across the channel; however, only in-focus cells are included in our analysis.

The images shown in Fig. 4 were taken under 1 mW illumination, limited by our fiber-coupled LED source intensity, with exposure times of $10\ \mu\text{s}$, and show flow rates of approximately $5\ \text{mm s}^{-1}$. We note that the above mentioned flow rate was kept low for demonstration of the imaging flow over a few frames. With this setup, we have imaged cells flowing at speeds of up to approximately $60\ \text{mm s}^{-1}$, which is comparable with flow rates of commercial high-speed imaging flow cytometers [25], using the full field of our camera with similar SNRs for the same acquisition time. Under these conditions, the maximum motion-induced blur is $600\ \text{nm}$, comparable to the diffraction limit in our imaging system.

Here, an enhancement of image absorption contrast is readily visible as well, with thicker cell areas having

higher absorption than the characteristic concave centers of the HRBCs. Phase contrast is apparent at cells' edges and centers. However, the phase contrast enhancement with m is limited by the axial depth of the channel. For example, overfocused planes of the sample imaged by O1 are underfocused by O2, washing out the phase contrast that would be obtained from imaging out-of-focus planes of a sample using a single objective. The phase contrast is therefore constant with respect to m . We note that this can be resolved by using a race-track multi-pass configuration instead of a linear configuration as depicted in Fig. 1.

We calculate the $\text{SNR}_m / \sqrt{\langle \hat{n} \rangle_0}$ at each pixel and its average value over a $120 \times 30\ \text{px}$ rectangle surrounding each cell center. The distributions of average $\text{SNR}_m / \sqrt{\langle \hat{n} \rangle_0}$ for approximately 400 cells imaged at $m = 1, 2$, and 4 are shown in Fig. 4 along with Gaussian fits to the distributions. A linear fit to the mean $\text{SNR}_m / \sqrt{\langle \hat{n} \rangle_{\text{in}}}$ as a function of m yields a measured average transmission $\eta = 0.968$ and an intercept resulting from phase contrast. The mean $\text{SNR}_m = 1.8, 2.9$, and 4.0 at $m = 1, 2$, and 4, respectively, which, as for the static case, shows a slight sub-linear enhancement due to loss in the optics. The increase in the distribution width as a function of m results from the contrast enhancement and demonstrates the increased sensitivity of the multi-pass absorption measurement. For a transmission $\eta = \eta_0 \pm \delta\eta$, we find that the width of the distribution in $\text{SNR} / \sqrt{\langle \hat{n} \rangle_0}$ should grow as $m\eta_0^{m-1}\delta\eta$ to first order in $\delta\eta$ and for high transmissivity, consistent with our measurement results. We further note that phase contrast and defocus through the flow channel can also contribute to the increased widths of the measured SNR distributions, however, these effects are minimized by selecting only in-focus cells for the analysis.

Enhancing the $\text{SNR}_1 \approx 1$ by a factor of two, as we do by going to $m = 2$, at constant illumination would require a four-fold longer camera exposure, which is impossible without blurring the image or reducing the flow rate. Multi-pass provides the requisite enhancement in SNR to enable faster flow and thus higher cell throughput at constant exposure, and these gains are further enhanced for the $m = 4$ configuration.

V. CONCLUSION

We presented a multi-pass imaging technique capable of operating at two and four passes using continuous wave illumination and standard cameras. We applied our multi-pass scheme to imaging flow cytometry to image human red blood cells at increased sensitivity when limited by the illumination source intensity. We demonstrated SNR enhancement by up to a factor of four, under flow conditions comparable to conventional high-speed instruments. Alternatively, such an enhancement can be used to speed up acquisitions by a factor of up to 16 for similar sensitivity. Our multi-pass technique approaches

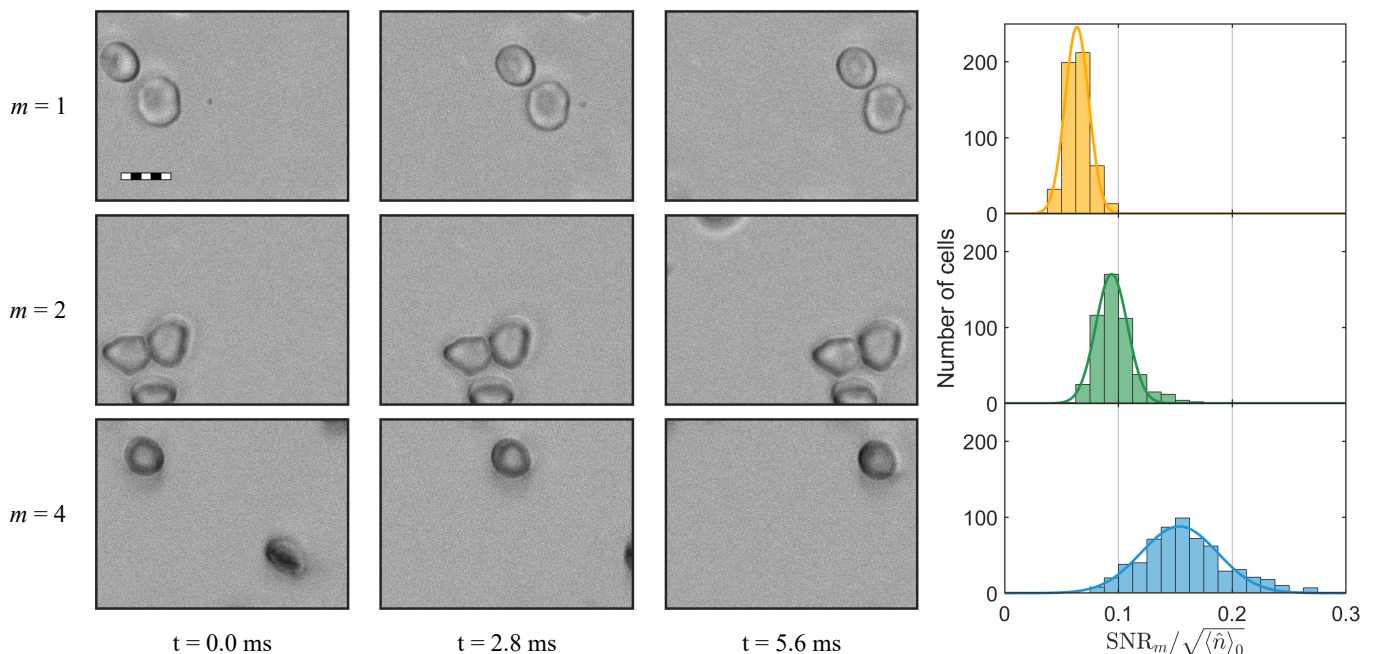


FIG. 4. Signal enhancement using multi-pass for red blood cells in flow. **Left:** HRBCs flowing left to right at $m = 1, 2,$ and 4 (top to bottom). The spatial and color scales are constant for all images ($10\ \mu\text{m}$ scale bar with $2\ \mu\text{m}$ ticks) to show enhancement in the absorption contrast. Flow rates are approximately $5\ \text{mm s}^{-1}$. The camera exposure time is $10\ \mu\text{s}$, 360Hz frame rate, and all pixels are normalized to their average value measured in the absence of cells. **Right:** histograms with Gaussian fits showing the average $\text{SNR}_m / \sqrt{\langle \hat{n} \rangle_0}$ for cells in flow. The signal includes a constant contribution from phase contrast and a contribution from absorption contrast that is enhanced by m . The sensitivity enhancement results in a broadening of the distributions.

close to the quantum limit for weak absorption measurements, while conventional (single-pass) absorption imaging is optimal for strong absorption, and both are achievable in our setup. Our technique presents a practical route for enhancing imaging sensitivity when the illumination is limited by the light source intensity, favoring multi-pass using classical light over proposed quantum light sources. Furthermore, it is easy to use and simple to implement, and thus could be widely deployed.

Funding This work was done as part of the Quantum Electron Microscope collaboration funded by the Gordon

and Betty Moore foundation.

Acknowledgments We would like to thank Cheri M. Hampton, Lawrence F. Drummy, Adam J. Bowman, Dara P. Dowlatshahi, and Stewart Koppell for helpful discussions.

Disclosures The authors declare no conflicts of interest.

Data availability Data underlying the results presented in this paper are not publicly available at this time but may be obtained from the authors upon reasonable request.

-
- [1] P. Hosseini, R. Zhou, Y.-H. Kim, C. Peres, A. Diaspro, C. Kuang, Z. Yaqoob, and P. T. So, Pushing phase and amplitude sensitivity limits in interferometric microscopy, *Optics Letters* **41**, 1656 (2016).
- [2] Y. Park, C. Depeursinge, and G. Popescu, Quantitative phase imaging in biomedicine, *Nature Photonics* **12**, 578 (2018).
- [3] S. Pirandola, B. R. Bardhan, T. Gehring, C. Weedbrook, and S. Lloyd, Advances in photonic quantum sensing, *Nature Photonics* **12**, 724 (2018).
- [4] P.-A. Moreau, E. Toninelli, T. Gregory, and M. J. Padgett, Imaging with quantum states of light, *Nature Reviews Physics* **1**, 367 (2019).
- [5] Y. Israel, S. Rosen, and Y. Silberberg, Supersensitive polarization microscopy using noon states of light, *Phys. Rev. Lett.* **112**, 103604 (2014).
- [6] N. Samantaray, I. Ruo-Berchera, A. Meda, and M. Genovese, Realization of the first sub-shot-noise wide field microscope, *Light: Science & Applications* **6**, e17005 (2017).
- [7] C. A. Casacio, L. S. Madsen, A. Terrasson, M. Waleed, K. Barnscheidt, B. Hage, M. A. Taylor, and W. P. Bowen, Quantum-enhanced nonlinear microscopy, *Nature* **594**, 201 (2021).
- [8] T. Li, F. Li, X. Liu, V. V. Yakovlev, and G. S. Agarwal, Quantum-enhanced stimulated brillouin scattering spectroscopy and imaging, *Optica* **9**, 959 (2022).

- [9] T. Juffmann, B. B. Klopfer, T. L. I. Frankort, P. Haslinger, and M. A. Kasevich, Multi-pass microscopy, *Nature Communications* **7**, 1 (2016).
- [10] B. B. Klopfer, T. Juffmann, and M. A. Kasevich, Iterative creation and sensing of twisted light, *Optics Letters* **41**, 5744 (2016).
- [11] S. C. Hur, H. T. K. Tse, and D. D. Carlo, Sheathless inertial cell ordering for extreme throughput flow cytometry, *Lab on a Chip* **10**, 274 (2010).
- [12] K. Goda, A. Ayazi, D. R. Gossett, J. Sadasivam, C. K. Lonappan, E. Sollier, A. M. Fard, S. C. Hur, J. Adam, C. Murray, C. Wang, N. Brackbill, D. D. Carlo, and B. Jalali, High-throughput single-microparticle imaging flow analyzer, *Proceedings of the National Academy of Sciences* **109**, 11630 (2012).
- [13] M. Doan, I. Vorobjev, P. Rees, A. Filby, O. Wolkenhauer, A. E. Goldfeld, J. Lieberman, N. Barteneva, A. E. Carpenter, and H. Hennig, Diagnostic potential of imaging flow cytometry, *Trends in Biotechnology* **36**, 649 (2018).
- [14] M. Motsch, M. Zeppenfeld, P. W. H. Pinkse, and G. Rempe, Cavity-enhanced Rayleigh scattering, *New Journal of Physics* **12**, 063022 (2010).
- [15] D. E. Chang, L. Jiang, A. V. Gorshkov, and H. J. Kimble, Cavity QED with atomic mirrors, *New Journal of Physics* **14**, 063003 (2012).
- [16] C. W. Helstrom, *Quantum Detection and Estimation Theory* (Academic Press, 1976).
- [17] A. S. Holevo, *Probabilistic and Statistical Aspects of Quantum Theory* (North-Holland Publishing Company, 1982).
- [18] S. L. Braunstein and C. M. Caves, Statistical distance and the geometry of quantum states, *Physical Review Letters* **72**, 3439 (1994).
- [19] E. J. Allen, J. Sabines-Chesterking, A. R. McMillan, S. K. Joshi, P. S. Turner, and J. C. F. Matthews, Approaching the quantum limit of precision in absorbance estimation using classical resources, *Phys. Rev. Research* **2**, 033243 (2020).
- [20] P. M. Birchall, E. J. Allen, T. M. Stace, J. L. O'Brien, J. C. F. Matthews, and H. Cable, Quantum optical metrology of correlated phase and loss, *Phys. Rev. Lett.* **124**, 140501 (2020).
- [21] S. Slussarenko, M. M. Weston, H. M. Chrzanowski, L. K. Shalm, V. B. Verma, S. W. Nam, and G. J. Pryde, Unconditional violation of the shot-noise limit in photonic quantum metrology, *Nature Photonics* **11**, 700 (2017).
- [22] A. Belsley, E. J. Allen, A. Datta, and J. C. Matthews, Advantage of coherent states in ring resonators over any quantum probe single-pass absorption estimation strategy, *Physical Review Letters* **128**, 230501 (2022).
- [23] P. M. Birchall, J. L. O'Brien, J. C. Matthews, and H. Cable, Quantum-classical boundary for precision optical phase estimation, *Physical Review A* **96**, 062109 (2017).
- [24] S. A. Koppell and M. A. Kasevich, Optimal dose-limited phase estimation without entanglement, arXiv preprint arXiv:2203.10137 (2022).
- [25] See for example, Amnis ImageStream^X Mk II, <https://www.luminexcorp.com/imagestreamx-mk-ii>.

Continuous wave multipass imaging: supplemental document

I. BRIGHT-FIELD MULTI-PASS ABSORPTION AND PHASE CONTRAST

The number of detected photons in bright-field multi-pass imaging of an object after m interactions is

$$\begin{aligned} \langle \hat{n} \rangle &= \left\langle \hat{\hat{n}} \right\rangle_{\text{in}} \eta^m \eta_{\text{rt}}^m \eta_D |e^{i\theta} + s e^{im\phi}|^2 \\ &= \left\langle \hat{\hat{n}} \right\rangle_{\text{in}} \eta^m \eta_{\text{rt}}^m \eta_D (1 + 2s \cos(m\phi - \theta) + s^2), \end{aligned} \quad (\text{S1})$$

where η is the transmission of the specimen, ϕ is the specimen phase shift, η_{rt} is the round-trip optical loss, η_D is the detection loss, θ is an auxiliary phase applied to the reference field (e.g. $\theta = \pi/2$ for a Zernike phase plate), s is the object scattered amplitude after m interactions, and $\left\langle \hat{\hat{n}} \right\rangle_{\text{in}} \equiv \langle \hat{n} \rangle_{\text{in}} / (|e^{i\theta} + s|^2)$, where $\langle \hat{n} \rangle_{\text{in}}$ is the average number of photons at the apparatus input. The signal-to-noise ratio (SNR) is hence

$$\begin{aligned} \text{SNR}_m &\approx \frac{\left| \langle \hat{n} \rangle - \langle \hat{n} \rangle_{\eta=1} \right|}{\sqrt{\langle \hat{n} \rangle + \langle \hat{n} \rangle_{\eta=1}}} \\ &= \frac{\sqrt{\eta_{\text{rt}}^m \eta_D \langle \hat{\hat{n}} \rangle_{\text{in}}}}{|e^{i\theta} + s|} \frac{2s(\cos(\theta) - \cos(m\phi - \theta)) + (1 + 2s \cos(m\phi - \theta) + s^2)(1 - \eta^m)}{\sqrt{(1 + s^2)(1 + \eta^m) + 2s(\cos(\theta) + \eta^m \cos(m\phi - \theta))}}. \end{aligned} \quad (\text{S2})$$

In the limit of a weak phase, weakly absorbing and scattering object, the SNR can be simplified. We drop terms of $O(s^2)$ and expand to first non-zero order in ϕ and the absorption, written in terms of the absorption per length α and the sample thickness z , such that $\eta = e^{-\alpha z}$. The result is

$$\text{SNR}_m \sim \sqrt{\frac{\langle \hat{n} \rangle_0}{2}} [s\phi^2 m^2 + \alpha z m] \quad (\text{for } \theta = 0), \quad (\text{S3})$$

$$\text{SNR}_m \sim \sqrt{\frac{\langle \hat{n} \rangle_0}{2}} [2s\phi m + \alpha z m] \quad (\text{for } \theta = \pi/2), \quad (\text{S4})$$

where the average squared-root photon flux without the object $\langle \hat{n} \rangle_0 \equiv \eta_{\text{rt}}^m \eta_D \langle \hat{n} \rangle_{\text{in}}$. Note that in our implementation of the multi-pass setup, the optical path changes between $m = 1, 2$, and 4 , resulting in an effective η_{rt} for each number of passes that does not build up as η_{rt}^m . This is particularly due to additional losses in defocusing objective O1 and optical elements, yielding a larger effective η_{rt} for $m = 1$, as well as the additional optical path for $m = 4$.

II. QUANTUM LIMIT FOR ABSORPTION ESTIMATION

In this section we give more details on the calculation of the QFI limit to absorption estimation (Equation 6 from the main text), denoting the maximum information available on η for any quantum probe and measurement which includes multiple interactions of the probe with the sample. The QFI for absorption estimation with quantum probes and m passes is given by [S1]

$$\mathcal{F}_{Q,m} = \langle \hat{n} \rangle_{\text{in}} m^2 \eta^{m-2} / (1 - \eta^m), \quad (\text{S5})$$

where $\langle \hat{n} \rangle_{\text{in}}$ is the mean total number of photons in the input probe state ρ_{in} . An expression similar to Eq. S5 was optimized in Ref. [S2] when $\tilde{m}_{\text{opt}} = -(2 + \mathcal{W}) / \ln \eta \approx -1.59 / \ln \eta$, where $\mathcal{W} \equiv W_0(-2/e^2) \approx -0.406$ is the main branch of the Lambert W function at $-2/e^2$ [S3]. Inserting \tilde{m}_{opt} into Eq. S5 we find the quantum limit to absorption estimation limited by number of input probe photons $\tilde{\mathcal{F}}_Q = \mathcal{F}_{Q,\tilde{m}_{\text{opt}}} / \langle \hat{n} \rangle_{\text{in}}$ (Eq. 6, main text),

$$\tilde{\mathcal{F}}_Q = -\frac{\mathcal{W}(2 + \mathcal{W})}{(\eta \ln \eta)^2} \approx \frac{0.65}{(\eta \ln \eta)^2}. \quad (\text{S6})$$

III. SATURATING THE CRAMER-RAO BOUND FOR MULTI-PASS LOSS SENSITIVITY

The uncertainty in η can be estimated from equation S1 using simple error propagation,

$$\Delta\eta = \left(\frac{\partial \langle \hat{n} \rangle}{\partial \eta} \right)^{-1} \Delta \langle \hat{n} \rangle = (\langle \hat{n} \rangle_{\text{in}} m \eta^{m-1} \eta_{\text{rt}}^m \eta_D)^{-1} \Delta \langle \hat{n} \rangle, \quad (\text{S7})$$

where, for absorption contrast, we take $\phi = \theta = 0$. Taking $\eta_D = 1$ and $\eta_{\text{rt}} = 1$, for a shot-noise limited measurement, $\Delta \langle \hat{n} \rangle = \sqrt{\langle \hat{n} \rangle_{\text{in}} \eta^m}$, and the inverse of the variance in η saturates the Cramer-Rao bound,

$$\frac{1}{\text{Var}(\eta)} = \langle \hat{n} \rangle_{\text{in}} m^2 \eta^{m-2} = \mathcal{F}_m. \quad (\text{S8})$$

-
- [S1] P. M. Birchall, E. J. Allen, T. M. Stace, J. L. O'Brien, J. C. F. Matthews, and H. Cable, Quantum optical metrology of correlated phase and loss, *Phys. Rev. Lett.* **124**, 140501 (2020).
[S2] P. M. Birchall, J. L. O'Brien, J. C. F. Matthews, and H. Cable, Quantum-classical boundary for precision optical phase estimation, *Phys. Rev. A* **96**, 062109 (2017).
[S3] R. M. Corless, G. H. Gonnet, D. E. Hare, D. J. Jeffrey, and D. E. Knuth, On the Lambert W function, *Advances in Computational Mathematics* **5**, 329 (1996).